COMMUNICATION

Reduced Grey Brookite for Noble Metal Free Photocatalytic H_2 Evolution

Received 00th January 20xx,
Accepted 00th January 20xx

DOI: 10.1039/x0xx00000x

Ewa Wierzbicka,[a] Marco Altomare,[a]* Mingjian Wu,[b,c,d] Ning Liu,[a] Tadahiro Yokosawa,[b,c,d] Dominik Fehn,[e] Shanshan Qin,[a] Karsten Meyer,[e] Tobias Unruh,[c,d,f] Erdmann Spiecker,[b,c,d] Leonardo Palmisano,[g] Marianna Bellardita,[g] Johannes Will,[b,c,d] and Patrik Schmuki[a,h,i]*

Herein we introduce for the first a reduced "grey" brookite TiO_2 photocatalyst, produced by thermal hydrogenation of brookite nanoparticles, that shows a remarkable noble metal free photocatalytic H_2 evolution. Its activity is substantially higher than that of other TiO_2 polymorphs, i.e. anatase or rutile, comparably sized and activated by hydrogenation under optimized conditions. Along with brookite powders, an oriented brookite single crystal was investigated as a defined surface to confirm the effects of the hydrogenation treatment. By a combination of Electron paramagnetic resonance (EPR), electron and X-ray characterization techniques applied to the powders and single crystal, we find that hydrogenation forms in brookite a defective crystalline surface layer rich in Ti^{3+} states. Amorphization effects, i.e. forming the so called "amorphous shell" as reported in previous work for black anatase TiO_2, were not detected. Overall, we provide experimental evidence that hydrogenation forms in brookite a surface strained zone with point defects that are mediators for electron transfer to H_2O, leading to a significantly enhanced noble metal free photocatalytic H_2 evolution in comparison to anatase.

Since the work of Fujishima and Honda in 1972,[1] titanium dioxide (TiO_2) has received ever growing attention in various research fields and particularly in photo-electrochemistry and photocatalysis.[2,3]

The most common TiO_2 crystalline forms are anatase, rutile and brookite.[4] These polymorphs offer comparable (photo-) chemical stability and non-toxicity, but only anatase and brookite feature conduction band (CB) minima that lie at a sufficiently more negative energy than the H_2O reduction potential ($H_2O \rightarrow H_2$).[5,6] In other words, photoexcitation of anatase or brookite TiO_2 can generate CB electrons that have a suitable "exit energy" to reduce water to H_2, while rutile TiO_2 is inactive (if no external electric bias is applied).

From a thermodynamic point of view, bulk rutile is more stable than anatase or brookite phases at room temperature, but anatase becomes the thermodynamically most stable polymorph when the particle size decreases below a few 10 nm.[7] This, along with a suitable band structure for H_2 evolution, explains why anatase TiO_2 nanomaterials have received huge attention in the last decades.

On the other hand, also brookite TiO_2 can in principle enable photocatalytic H_2 evolution (as well as other photocatalytic reactions of environmental interest[5,6,8–17]) but its synthesis as pure polymorph, free from rutile or anatase contaminations, is laborious. Reliable protocols for the preparation of pure brookite nanomaterials via synthetic routes at mild temperatures and pressures have become available only recently.[8,11,18,19] Hence, brookite has been investigated in a comparably limited number of studies.

Regardless of the polymorph, charge recombination and sluggish charge transfer remain common limitations translating into low photocatalytic performances. These issues can be overcome by decorating TiO_2 with a noble metal (Pt, Pd, Au) or other alloy co-catalytic nanoparticles (NPs).[20–26] Such NPs can enable a significant enhancement of the H_2 evolution rate by providing efficient charge separation and transfer through the formation of localized Schottky junctions at the TiO_2 surface.[27] Such metals may also provide catalytic

[a] Department of Materials Science WW4 LKO, Friedrich-Alexander University of Erlangen-Nuremberg (FAU), Martensstrasse 7, 91058 Erlangen, Germany
[b] Department of Materials Science Institute for Micro- and Nanostructure Research IMN, Friedrich-Alexander University Erlangen-Nuremberg (FAU), Cauerstrasse 3, 91058 Erlangen, Germany
[c] Center for Nanoanalysis and Electron Microscopy (CENEM), Friedrich-Alexander University of Erlangen-Nuremberg (FAU), Cauerstrasse 3, 91058 Erlangen, Germany
[d] Interdisciplinary Center for Nanostructured Films (IZNF), Friedrich-Alexander University of Erlangen-Nuremberg (FAU), Cauerstrasse 3, 91058 Erlangen, Germany
[e] Department of Chemistry and Pharmacy, Inorganic Chemistry, Friedrich-Alexander University Erlangen-Nürnberg (FAU), Egerlandstrasse 1, 91058 Erlangen, Germany
[f] Department of Physics, Institute for Crystallography and Structural Physics, Staudtstrasse 3, 91058 Erlangen, Germany
[g] "Schiavello-Grillone Photocatalysis Group", Engineering Department, University of Palermo, Viale delle Scienze, 90128 Palermo, Italy
[h] Department of Chemistry, King Abdulaziz University, Jeddah, Saudi Arabia
[i] Regional Centre of Advanced Technologies and Materials, Department of Physical Chemistry, Faculty of Science, Palacky University, Slechtitelu 11, 783 71 Olomouc, Czech Republic

† Electronic Supplementary Information (ESI) available: [details of any supplementary information available should be included here]. See DOI: 10.1039/x0xx00000x

effects, e.g. active surface sites to catalyze hydrogen recombination ($2H^0 \rightarrow H_2$).[28]

More recently, an alternative path to metal co-catalyst decoration has been pioneered by Liu and co-workers, that is, reduced anatase or mixed anatase/rutile phase TiO_2 nanoparticles, treated under "mild" hydrogenation conditions to form so called "grey" titania, were found to yield stable photocatalytic H_2 generation in the absence of any noble metal co-catalyst.[29–38] This activation was associated with the formation of surface oxygen vacancies (V_Os) and Ti^{3+} states that can act as intrinsic co-catalytic sites for H_2 evolution.[39–43]

The nature of such defects (V_Os and Ti^{3+} states) vary depending on structural features (e.g. whether the defects are formed at the surface, subsurface or in the bulk, site coordination etc.) and energetics of the associated states. The formation of states located deep (~ 0.9 eV) below the CB has been reported for rutile TiO_2. In the case of anatase, such defect states are shallow, i.e. < 0.1 eV below the CB.[44,45] Transient absorption (TA) spectroscopy studies of reduced brookite showed that excited electrons can be trapped at "moderate depth" defects located about 0.4 eV below the brookite CB.[44,45] Such parameters (locations, energetics) determine in turn whether defects are photocatalytically active or not. For example, it was shown that the presence of under-coordinated surface Ti_{5c} ions (shallow states) in anatase can stabilize extra charge at the surface, making it available for charge transfer to adsorbates.[46] Studies on O-deficient titania (produced e.g. by hydrogen annealing) show that oxygen vacancy formation is slightly more favourable in anatase than rutile, while Ti interstitials form more easily in rutile than anatase.[47] Ti interstitials energy places much deeper electron traps than other Ti ions (> 1eV), so their energy level location is below the H_2/H_2O redox potential, and make the photocatalytic activity of the reduced rutile negligible.[47,48]

Despite the potential contribution to photocatalysis originating from Ti^{3+} and V_O species, the understanding of structure and energetics of defects is still elusive for brookite, i.e. the least known TiO_2 polymorph. In this context, brookite is particularly interesting for studying the effects of point defect engineering since its conduction band edge position is placed above that of anatase and rutile,[5,6,49,50] i.e. a variety of sub CB states can in principle be formed that are higher in energy than H_2O/H_2 redox potential.

Herein, we investigate the reduction of pure brookite nanopowders and single crystals by thermal hydrogenation. We hydrogenate brookite nanoparticles produced by thermohydrolysis of $TiCl_4$[10,11] and compare their performance to grey (hydrogenated) anatase and rutile TiO_2 nanoparticles. To best of our knowledge, a comparison between the photocatalytic activity of hydrogenated pure brookite, anatase and rutile TiO_2 phases has not been reported yet. We observe that while rutile, untreated or hydrogenated, exhibits negligible H_2 evolution, both brookite and anatase show a pronounced activity enhancement after hydrogenation at 500°C. Nonetheless, under optimized hydrogenation conditions, the activity of brookite NPs is almost 3 times higher than that of anatase powders. Investigations on brookite single crystals reveal surface point defects such as (V_Os and Ti^{3+} states) and surface strain effects that are considered crucial towards co-catalyst free photocatalysis. Interestingly, compared to the 1 h long treatment needed to activate anatase, brookite nanopowders can reach a significantly higher activity for hydrogenation times as short as 5-10 minutes. Such hydrogenation treatment is found neither to alter the pure brookite phase composition (i.e. no phase transition) nor to induce amorphization effects (so called "amorphous shell" as reported in previous work for "black" anatase TiO_2).[37,51,52] On the other hand, over-treating brookite (T > 500°C or treatments > 10 min) results in a dramatic deactivation, which was found to correspond to a phase transition into rutile TiO_2.

Results and discussion

TiO_2 brookite powders were synthetized by a thermal hydrolysis approach as described elsewhere.[10,11] These nanopowders were then exposed to a hydrogenation treatment in a flow furnace at temperatures between 300 and 600°C in pure H_2 (or in air, to produce reference materials). Reference experiments were also conducted with commercially available anatase or rutile NPs, untreated or annealed in H_2. Experimental details can be found in the Supporting Information.

Figure 1a shows SEM images of the powders herein studied. As-synthetized brookite and as-received anatase show a comparable nanoparticle size of ~ 30 nm. Rutile nanoparticles are slightly larger, i.e. ~ 60 nm.

The TEM image of the powder in **Figure 1a** shows that as-synthesized brookite appears in the form of aggregates of nanocrystals with average size of a few tens of nm. After sonication in water, brookite dispersions show a remarkable stability, as sonication can convert the aggregates into individual highly dispersed nanocrystals (see Supporting Information, TEM sample preparation). When observed by TEM, these NPs feature an undefined shape and high surface roughness. In order to assess the photocatalytic performance of these brookite suspensions, we benchmarked them against suspensions of comparably sized anatase or rutile powders (SEM images in **Figure 1a**). The photocatalytic experiments were carried out under illumination provided by a solar simulator (AM 1.5 G, 100 mW cm^{-2}) and using methanol (50%) as a sacrificial agent. The amount of evolved H_2 was determined after fixed illumination time intervals by gas chromatography.

Figure 1b,c show the H_2 evolution rate of the suspensions of the different polymorphs, before and after hydrogenation, for a range of different conditions. The samples are labeled according to their phase composition and atmosphere, temperature and duration of the thermal treatment as following: "B" = brookite, "A" = anatase, "R" = rutile; "H2" = hydrogen, "air" = air. The temperature is expressed in °C while the treatment time in hours (h) or minutes (min).

One can see from **Figure 1b** that as-synthesized untreated brookite ("white" brookite) shows a relatively poor H_2 evolution performance (30 µmol h^{-1} g^{-1}), which is however

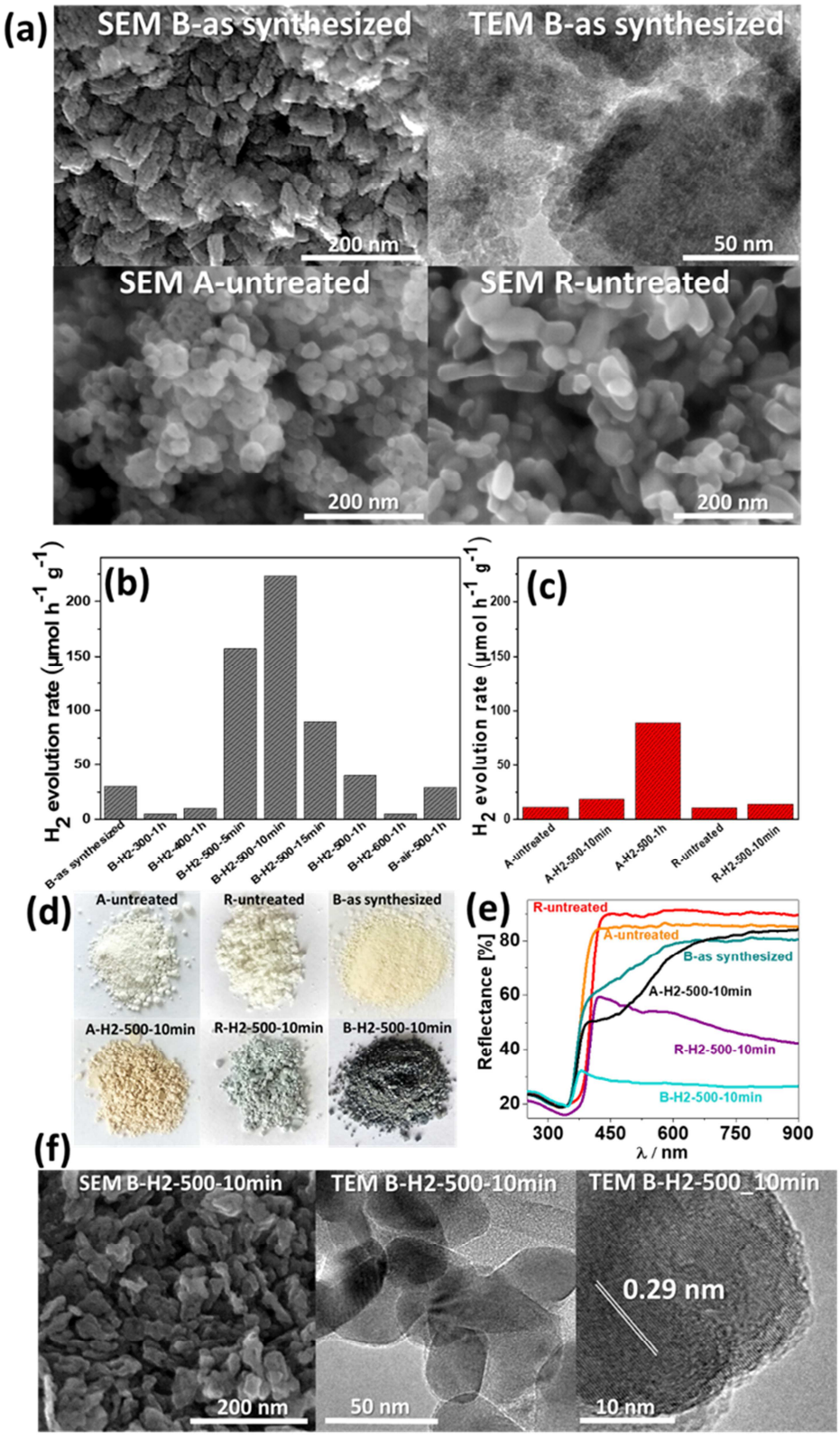

slightly higher than that of untreated anatase or rutile (11 and 10 µmol h^{-1} g^{-1}, respectively; **Figure1b)**.

To find the optimal conditions for brookite activation, various hydrogenation temperatures and times were screened.

Figure 1 (a) SEM of untreated brookite anatase, rutile and TEM of as-synthesized brookite (b) Photocatalytic H_2 evolution rates (from H_2O: methanol 50:50 vol.% solutions under AM 1.5, 100 $mWcm^{-2}$ illumination) of untreated brookite, of different hydrogenated brookite NPs and of a reference brookite sample treated in air. (c) Photocatalytic H_2 evolution rate of anatase and rutile powders measured under comparable conditions as in (b). (d) Optical images of untreated and 10 min hydrogenated (500°C) anatase, rutile and brookite nanopowders. (e) Integrated light reflectance spectra of powder presented in (d). (f) SEM and TEM of 10 minutes hydrogenated brookite particles (500°C).

Brookite nanopowders treated at 300°C or 400°C for 1h (samples B-H2-300-1h and B-H2-400-1h) show a drop of activity compared to untreated powders. This, as evident from EPR results discussed later, suggests that hydrogenation temperatures ≤ 400°C generate minute concentration of defects (V_O and Ti^{3+}) in the brookite nanoparticles, likely of a detrimental nature, i.e. that act as charge recombination centers.

In the case of hydrogenated rutile powders, for any hydrogenation condition investigated, we measured only negligible amounts of H_2 generated (**Figure 1c**).

On the contrary, for anatase, as also outlined in our previous work,[40] we found an optimized activation when the powders are hydrogenated at 500°C for 1h. Such a treatment of anatase nanopowders provides enhanced and stable photocatalytic H_2 evolution without the use of any noble metal co-catalyst, and this result is herein confirmed (**Figure 1c**).

A distinct increase of the H_2 production can be observed for brookite as well, for example when these powders also are treated in H_2 gas at 500°C for 1h (sample B-H2-500-1h). However, an even more pronounced activity enhancement can be achieved for brookite through shorter hydrogenation times, i.e. 5-10 minutes, which lead to a "grey" brookite photocatalyst that can provide H_2 evolution rates as high as 223 μmol h^{-1} g^{-1}, as observed for the powders treated for only 10 minutes (sample B-H2-500-10min). Note that such activity is almost 3 times higher than that of anatase powders hydrogenated under optimized conditions (89 μmol h^{-1} g^{-1}, sample A-H2-500-1h),[40] and the performance gap is even more stunning if comparison is made to anatase powders hydrogenated for comparably short times (10 min): an activity of 11 μmol h^{-1} g^{-1} was measured for sample A-H2-500-10min. These findings, overall, suggest that the "grey" brookite polymorph is clearly more effective than "grey" anatase or "grey" rutile.

For brookite powders hydrogenated under optimized conditions (500°C, 10 min), reproducible hydrogen evolution was obtained in repeated photocatalytic tests (**Figure S1**). This sample (B-H2-500-10min) was also tested for overall water splitting (in pure water), but no significant amounts of H_2 and O_2 could be detected after 24 h AM 1.5 solar illumination. This is similar to anatase. In both cases, the grey materials only in the presence of methanol (hole scavenger) can produce H_2. In the absence of methanol or of a suitable hole transfer (O_2 evolution) catalyst, photo-produced holes likely accumulate in the semiconductor and increase charge recombination, thereby also hampering H_2 evolution.[53–55]

For longer hydrogenation times (e.g. 1h, sample B-H2-500-1h) or higher temperatures (e.g. 600°C, sample B-H2-600-1h) a drastic reduction of the brookite photocatalytic activity is observed. This, as evidenced below by EPR, Raman and XRD results, can be ascribed to the beginning of a phase transition to rutile that is accompanied by the formation of detrimental Ti^{3+} defects. Moreover, brookite NPs treated in air at 500°C for 1h (sample B-air-500-1h) shows a poor activity. This confirms that the improved H_2 evolution efficiency of hydrogenated brookite is not related to the treatment temperature alone, but rather to the combination of a H_2 environment with optimized temperature (500°C) and duration (10 min) of the treatment.

Optical pictures and UV-Vis diffuse reflectance spectra for untreated and hydrogenated brookite, anatase and rutile powders are shown in **Figure 1d and 1e**, respectively. The optical images show that every polymorph darkens upon hydrogenation. It is however evident that brookite powders darken the quickest, despite the same treatment time (10 min).

The UV-Vis spectra of untreated powders show the typical UV absorption due to TiO_2 band gap excitation. The absorption onset for rutile is slightly shifted to longer wavelengths than those of anatase and brookite, in line with the E_g values of ~3.0, 3.2 and 3.3 eV for rutile, anatase and brookite TiO_2, respectively, and with band gap estimation from photo-electrochemical measurements discussed below.[5,6] All the polymorphs show a clear increase of the optical extinction in the visible range, which is well in line with their pale to dark grey color. Darkening of the TiO_2 powders by reduction/hydrogenation has been widely discussed in literature for colored (e.g. blue, grey or black) titania,[40,41,51,56] and can in general be ascribed to the formation of Ti^{3+}-O_v species that behave as color centers. The darker color of hydrogenated brookite powders along with the higher optical extinction in the visible spectral range suggests the formation of a higher density of Ti^{3+} states in brookite than in other polymorphs, as also confirmed by EPR results (below).

The SEM and TEM data in **Figure 1f** show the morphological and crystallographic features of hydrogenated brookite (500°C, 10 min; sample B-H2-500-10min). When comparing the SEM images in **Figure 1f** and **Figure 1a**, one may notice that the brookite particles become smoother at the surface and more round in shape after the H_2 treatment. This is also evident from high-resolution TEM images (**Figure 1f**). Interestingly, the hydrogenation leads also to more uniform, defined crystalline particles, showing lattice fringes with spacing of 0.29 nm, which can be attributed to the (121) brookite lattice planes.[18,57] The particles appear fully crystalline and do not feature any "seemingly" amorphous location (or "shell"), as frequently reported for hydrogenated anatase particles.[51] Besides, the morphology of anatase and rutile nanopowders were not affected by the hydrogenation treatment (cf. **Figure S2** with **Figure 1a**).

To assess the nature of the defects induced by hydrogenation, X-band EPR spectra were taken at 95 K for untreated brookite, anatase, and rutile as well as for brookite, anatase, and rutile powders treated in H_2 at 500ºC for 10 min (**Figure S3** and **Figure 2a**, respectively).

The untreated anatase, brookite, and rutile samples show a minor paramagnetic response, which can be assigned to common lattice defects in very low concentrations (**Figure S3**).

After treatment at 500°C in H_2 for 10 min, all titania polymorphs are found to feature paramagnetic species with different peak signatures. In general, it is clear from the spectra in **Figure 2a** that brookite (sample B-H2-500-10min) contains the largest density of defects compared to the

anatase and rutile polymorphs (samples A-H2-500-10min and R-H2-500-10min, respectively). The EPR spectrum of brookite (B-H2-500-10min) shows two isotropic signals, ascribed to two different species, with g values g_1 = 2.00 (4.2%),[58] corresponding to bulk Ti^{3+} defects, and g_2 = 1.93 (95.8%), assigned to highly disordered surface exposed Ti^{3+}.[59,60] The contributions of these two species are determined by simulation as shown in **Figure S4**.

Under identical measurement conditions, the hydrogenated anatase sample (A-H2-500-10min) displays three paramagnetic species, all of which being too low in intensity for a proper assignment, thus indicating that a 10 min hydrogenation treatment produces in anatase a comparably small defect density.

The hydrogenated rutile sample (R-H2-500-10min) features one low-intensity isotropic signal at g = 1.96, ascribed either to Ti^{3+} centers introduced at regular lattice positions or interstitial Ti^{3+} centers (very similar g-tensor values).[59,61]

These findings, in line with literature,[33,60,62] suggest that:

(i) Key for the high H_2 evolution activity observed for defect engineered anatase and brookite is the presence of surface Ti^{3+} states (g = 1.93). Note that these surface exposed paramagnetic states in the investigated brookite sample (B-H2-500-10min) are dominant (95.8%) compared to bulk defects (4.2%), as determined by simulation (supporting information, **Figure S4**);

(ii) For the same hydrogenation time of 10 min, the defect density produced in anatase is clearly much lower than for brookite – this for both lattice and surface defects. This is in line with a lower photocatalytic activity of anatase. As shown in earlier work, surface exposed defects are the co-catalytic sites for H_2 evolution. Defects formed in brookite appear to be of a comparable electronic nature to those introduced in anatase. Both "grey" modifications provide a comparable signature, as was reported in previous work for "grey" anatase;[40,62,63]

(iii) Defects produced in rutile are of a different electronic nature than defects generated in brookite or anatase. Particularly, hydrogenated rutile does not feature the typical signature assigned to surface exposed Ti^{3+} states in anatase or brookite. This may be ascribed to the different nature of the energetics of defects (interstitial Ti^{3+}) in the rutile polymorph,[47,61,64,65] indicating that these deeper defects (electron traps) are not able to mediate charge transfer to the environment (their energy level is below the H_2/H_2O redox potential).[47,48]

Notably, for brookite, when increasing the treatment time from 10 min to 1 h at the same temperature of 500°C, the EPR signature of produced defects dramatically changes: the two isotropic signals with g values g_1 = 2.00 and g_2 = 1.93 vanish (bulk and surface Ti^{3+} states, respectively), while new isotropic species can be observed featuring g = 1.96 (see simulated spectrum **Figure S5**). Note that the same signature is detected for hydrogenated rutile (R-H2-500-10min, spectrum in **Figure 2a**). The appearance of the new signal goes along with a beginning phase transition from brookite to rutile, as confirmed by Raman results discussed below. In other words, the observed shift in paramagnetic signal confirms that the phase transformation cause also conversion of "moderate depth" Ti^{3+} defects in brookite into "deep trapping states" in rutile, these located below the H_2 evolution potential.[44,45,47,66] Plausibly, this phase transition is the main cause for the decrease of photocatalytic H_2 evolution activity of "over-treated" brookite (**Figure 1b**).

EPR measurements of brookite powders treated in H_2 at a lower temperature (400°C) or treated in air do not show any significant appearance of paramagnetic species (**Figure 2b**). This observation is in line with the photocatalytic results, i.e. neither hydrogenation at T ≤ 400°C nor annealing in air provide defects that can act as intrinsic co-catalyst sites for H_2 evolution.

We carried out a series of photo-electrochemical measurements to substantiate the origin of the enhanced activity of hydrogenated brookite. We produced photo-electrodes made of different powders (untreated brookite, hydrogenated brookite (500°C, 10 min) and untreated anatase – see SI for experimental details), and performed wavelength dependent photocurrent measurements, determined the samples' bandgap and acquired photocurrent transients at fixed illumination wavelength. The results, compiled in **Figure S6**, show that:

- Incident photon to current efficiency (IPCE) (**Figure S6a**): untreated brookite delivers smaller photocurrents than anatase across the entire absorption range. Grey brookite, however, yields the highest IPCE particularly for short wavelengths e.g. λ ≤ 350 nm, likely due to an improved electron conductivity upon hydrogenation (higher density of oxygen vacancies). In any case, only UV light absorption translates into photocurrent, indicating that hydrogenation does not narrow the semiconductor band gap or, in other words, that there is no photocurrent contributing states in the band gap.
- Band gap estimation (**Figure S6b**): the E_g of grey brookite is equivalent to that of untreated brookite powders, i.e. ca. 3.3-3.4 eV, but is larger than that of anatase (ca. 3.1-3.2 eV). This confirms that the conduction band minimum (CBM) of brookite is situated above that of anatase, hence providing a larger overpotential for electron transfer for water reduction and H_2 evolution.
- Photocurrent transients (**Figure S6c**): hydrogenation of brookite leads to a higher photocurrent compared to untreated powders owing to a higher electron conductivity.[36,67,68] Moreover, the transient profile for grey brookite indicates a trap filling mechanism, hence proving that hydrogenation introduces point defects that act as electron trap states (responsible for H_2 evolution under photocatalytic conditions).

Crystallographic information for the different powders were obtained from Raman spectroscopy. Data for as-synthesized brookite and for powders treated at 500°C for short time annealing (5, 10, 15 minutes) are compiled in **Figure 2c**.

For the brookite powder annealed for 5, 10 and 15 minutes at 500°C, only the presence of brookite phase can be detected. The characteristic Raman active modes in the vibrational

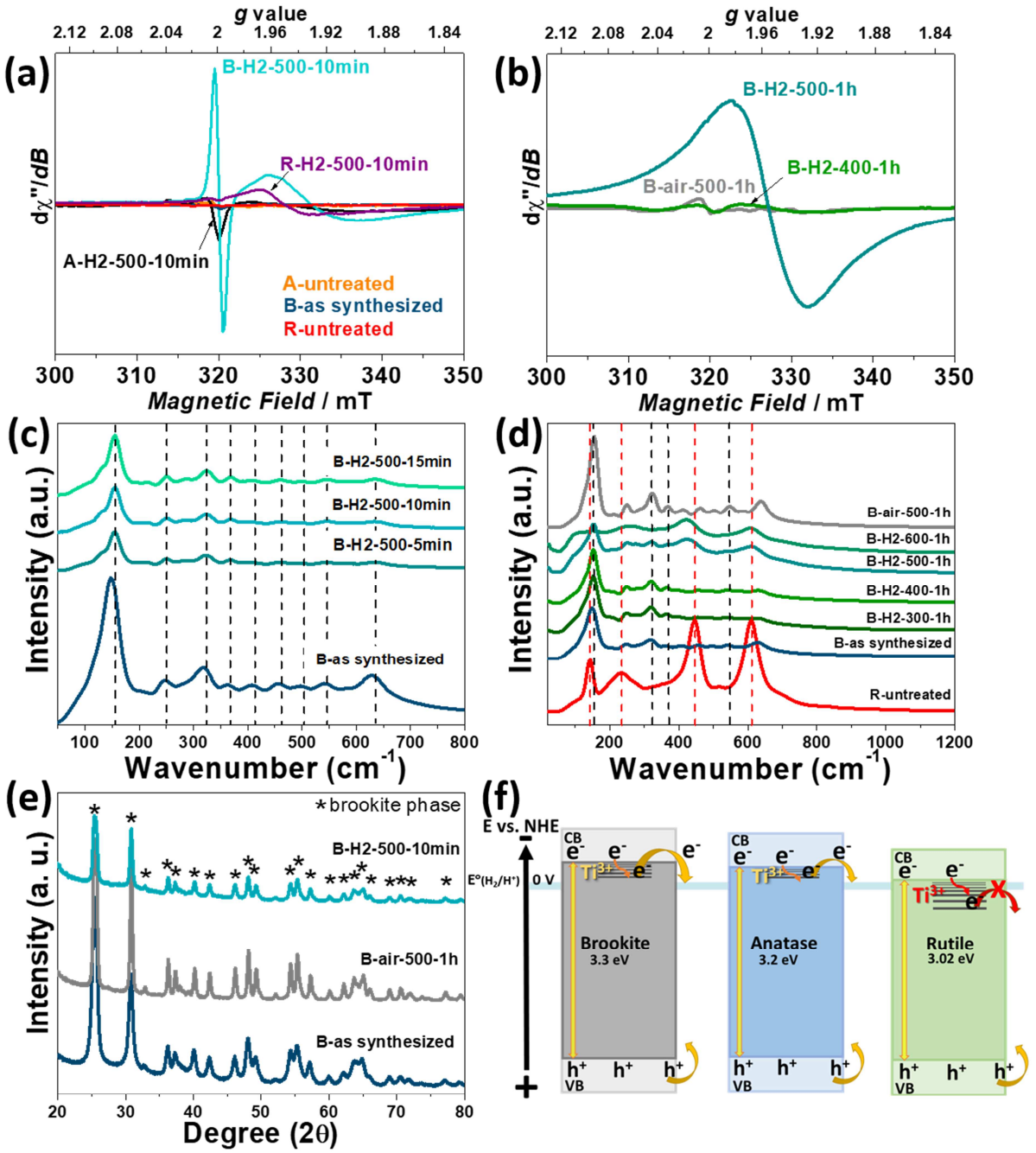

Figure 2 EPR spectra of (a) untreated brookite, rutile and anatase and of 10 min-hydrogenated powders at 500°C; (b) 1 h annealed brookite in air at 500°C, hydrogen at 400°C and 500°C. (c) Raman spectra of pristine brookite and of brookite hydrogenated at 500°C for 5, 10 and 15 minutes. (d) Raman spectra of pristine brookite and rutile, and of powders 1h annealed at temperatures between 300 and 600°C in hydrogen or air. (e) XRD spectra of pristine brookite and of brookite annealed at 500°C in hydrogen (10min) or air (1h). (f) Schematic drawing of the energy diagrams for hydrogenated anatase, brookite and rutile.

spectrum of brookite samples can be assigned as follows: A1g (153, 247, 412, 636 cm-1), B1g (323, 502 cm-1), B2g (366, 461 cm-1), and B3g (545 cm-1).69 The peak positions of the annealed samples show a small blue shift compared to the untreated powder. Such a shift may be due to the merge of adjacent nanocrystals during the heat treatment, forming more uniform particles and larger crystalline domains.70 Indeed SEM and TEM observations corroborate that hydrogenation leads to more uniform and larger particles.

Figure 2d shows the Raman spectra of brookite powders treated at different temperatures (300-600°C range) or in different atmospheres (H_2 vs. air). The spectrum of untreated rutile is also shown as a reference.

Samples treated at 300 and 400°C (B-H2-300-1h and B-H2-400-1h) show the typical vibrational spectrum of brookite. The 1 h long hydrogenation at temperatures of 500ºC or higher (B-H2-500-1h and B-H2-600-1h) leads however to a gradual phase transformation to rutile. The phase transition is evident by comparison to the rutile reference spectrum that features as main modes: B_{1g} (143 cm^{-1}), A_{1g} (611 cm^{-1}), E_g (448 cm^{-1}) and an undefined signal at 235 cm^{-1}.[69] Thermal conversion of brookite into rutile is well documented in previous literature.[4]

Interestingly, our results also show that the hydrogen atmosphere accelerates the phase transformation of brookite to rutile while air annealing at comparable temperatures (e.g. at 500°C, sample B-air-500-1h) does not lead to any phase change detectable by Raman spectroscopy, in agreement with reports on defect facilitated phase transitions.[70]

To further confirm the findings, we carried out XRD measurements of differently treated brookite samples. **Figure 2e** shows XRD patterns of the as-produced brookite TiO_2 and of powders annealed at 500°C in air for 1 h, or in pure hydrogen for 10 minutes. All samples show only the characteristic diffraction pattern of pure brookite (PDF card No. 00-029-1360), with main reflections at 25.3°, 30.8°, 36.2°, 48.0°, 55.2° and 64.1°. For the heat treated samples, a decrease of the full-width at half maximum (FWHM) is observed that reflects an improvement of the powder crystallinity, e.g. larger crystalline domains or larger particle sizes are obtained by annealing compared to the as-produced powers.

In other words, above results show that – as for anatase[33,40–42] – also for brookite, both nature and density (concentration) of defects produced by thermal hydrogenation have a remarkable effect on the photocatalytic H_2 evolution performance.

In this context, it is worth to point out that "moderate" H_2 treatment (e.g. at 500°C) in anatase creates electronic states associated to point defects (V_Os and Ti^{3+} states) that are energetically located right below the conduction band edge (**Figure 2f**).[37,46,51,52] This seems also to hold for brookite. However, among the TiO_2 polymorphs, brookite has the energetically highest conduction band edge (-0.57 – -0.54 V vs. NHE at pH 7), followed by anatase (-0.48 – -0.35 V), and by rutile (-0.37– -0.35 V).[6,10,71] Thus, in accord with literature[72], the weak activity of rutile can be ascribed to its CB energy level, which does not provide a suitable exit energy for photo-promoted electrons to reduce H_2O or H^+ to H_2. Hydrogenated rutile powders show virtually the same negligible activity as untreated samples (**Figure 1c**), this because any intra-gap defect state introduced with hydrogenation is even lower in energy than the CB minimum, and thus cannot contribute to H_2 evolution.[44,47,48]

The situation is different for anatase and brookite, i.e. electrons on the intra-band gap states located in energy close to the CB minimum have sufficient energy to reduce H_2O to H_2, and can hence provide, as observed, co-catalyst free activity and a performance enhancement compared to untreated counterparts (**Figure 1b,c**).

In order to elucidate further the role of introduced defects, we H_2-treated at 500°C a 5 x 5 mm^2 brookite single-crystal (surface orientation [100], orthorhombic; SurfaceNet GmbH, Germany). This single crystal, both in the hydrogenated and non-hydrogenated form, was studied by (scanning) transmission electron microscopy (S/TEM) techniques including high-resolution STEM imaging, Selected Area Electron Diffraction (SAED), and spatially resolved Electron Energy Loss Spectroscopy (EELS), as well as by X-ray Diffraction (XRD) and X-ray Reflectivity (XRR).

For electron microscopy, a cross-section lamella was prepared perpendicular to the [100] direction of the hydrogenated brookite single crystal surface with standard focused ion beam (FIB) lift-out technique. Care was taken to preserve the native surface structure (see experimental section in the Supporting Information).

Figure 3a shows a cross-section STEM bright-field (BF) overview image of the brookite surface. A rough surface is clearly revealed. STEM-BF as well as high angle annular dark filed (STEM-HAADF) images of the top layer are compared in **Figures 3b** and **c**). While the BF image highlights the crystalline nature of the interface, the HAADF image contrast is mainly sensitive to mass-thickness[73] and it reveals a 13 nm surface layer with lower intensity. The presence of this surface layer is also apparent from SAED and XRR measurements (examined below). Beside the surface features, some intrinsic defects such as stacking faults, voids and α-Fe precipitates are present in the *bulk* of the crystal. Iron is a common impurity in natural brookite single crystals and therefore its presence cannot be avoided. Note however that Fe species are relatively deep in the bulk of the brookite single crystal (e.g. a few 100 nm deep or more, EDX in **Figure S7**), and their presence likely does not affect the surface properties of the single crystal and the effect of the hydrogenation treatment.

Since the surface is more relevant to photocatalysis, analysis of these bulk defects is provided in the SI (see further **Figure S7**), while in the following we focus on the crystal surface features.

In order to compare the crystalline surface layer with the bulk structure of the brookite single crystal, SAED patterns were taken at a defect-free bulk location of the sample and compared to the signal originating from the defective outer layer. The resulting diffraction patterns, displayed in **Figures 3d** and **e**, exhibit no detectable differences in their Bragg peak positions and their patterns are both in-line with a single-crystalline brookite phase (a = 9.184 Å, b = 5.447 Å, c = 5.145 Å).[74] Differences in the peak intensities originate from the different amount of scattering material due to e.g. the smaller SAED aperture utilized for the pattern taken in the narrow defective zone. A SAED pattern of the interface with a higher angular resolution (longer camera length) as well as a line cut along the 00L direction is compiled in **Figure S8**. Because of the finite layer thickness, Laue fringes[75] evolve around the Bragg Peaks. The asymmetric appearance of the Laue fringes originates from a slight misorientation of the lamella with respect to a perfect [011] zone axis. However, it is still reasonable to estimate the surface layer thickness from the fringe spacing, which leads to a vertical crystalline layer dimension of ~ 12 nm. This again demonstrates that the outermost layer exhibits a single crystalline brookite phase nature, characterized however by a lower density compared to the brookite bulk.

X-ray Diffraction was used to probe the brookite single crystal surface before and after the hydrogenation. Bulk sensitive Bragg Brentano measurements reveal the surface normal crystal structure – the measurements are combined with *i)* surface sensitive grazing incidence data that yield the in-plane crystal structure, and *ii)* X-ray reflectometry (XRR) studies that

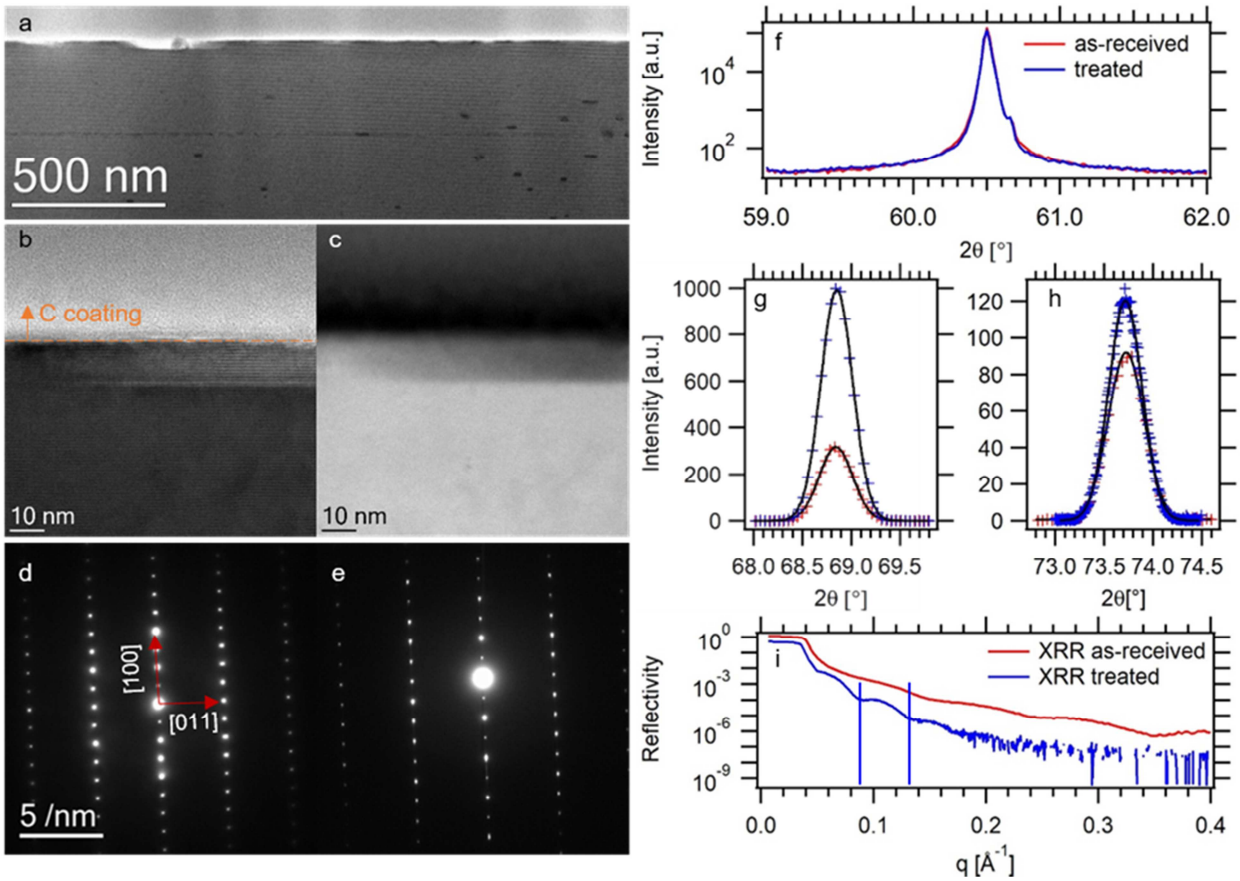

Figure 3 (a) Overview STEM BF image of the hydrogenated brookite lamella in cross-sectional view prepared by a FIB lift-out. (b) and (c) High resolution STEM BF and HAADF image of the brookite/ambient interface, respectively. (d) and (e) SAED patterns of the bulk and the brookite/ambient interface, respectively. (f) Enlarged logarithmic view of the (600) brookite Bragg-Peak (XRD) before (red) and after (blue) hydrogenation. Comparison of the (040) (g) and (004) (h) in-plane Bragg-Peaks (XRD) before (red) and after (blue) hydrogenation. The black solid lines are the best Gaussian fits. (i) XRR curves before (red) and after (blue) hydrogenation. The blue vertical lines indicate the characteristic spacing of apparent Kiessig fringes. Note the XRR curves are shifted vertically for clarity.

give insight into the surface normal density profile with sub-nm resolution.[76] All mentioned techniques have in common that the signal is averaged over the whole illuminated specimen area in the range of some mm^2, thus complementing the results from electron microscopy which picture the atomic scale but at a very local specimen volume (typical TEM lamella µm^2 x 100 nm). The influence of hydrogenation on the surface normal crystal structure is summarized in **Figure 3f** (enlarged view of the brookite (600) reflection) and **Figure S9** (full 2θ range). The signal, which is dependent on the respective reflection from a vertical depth of typically several µm (Bragg-case extinction length), shows i) no detectable change of lattice parameter along the surface normal brookite crystal structure, ii) no transformation to rutile phase, where the most intense peaks would evolve around 2θ = 27.43°, 36.08°, 54.32° or 69.0°[77] and iii) an increment of the α-Fe 110 peak around 44.7° arising from the growth of the Fe precipitates detected by electron microscopy. Thus, XRD confirms that the hydrogenation treatment of the brookite single crystal at 500°C does not cause a brookite-to-rutile phase transformation, which is in-line with the nanopowder findings reported above.

We further characterized the untreated and hydrogenated single crystal by Grazing Incidence In-plane Diffraction. By impinging the specimen with a parallel beam under an angle below the one for total external reflection, an evanescent wave, with rapidly decaying amplitude inside the specimen, probes the material vertically with a depth of only a few hundred Å, thus giving rise to a much higher surface sensitivity than ordinary θ/2θ diffraction.[78] Here, we focused on the influence of hydrogenation on the (040) and (004) Bragg Peak. The results are summarized in **Figures 3g** and **h**). While the Bragg Peak position stays constant and is limited by the instrumental resolution, the peak intensity increases after hydrogenation. This increment can be attributed to lattice distortion, which is in average much more pronounced along the [010] as compared to the [001] direction.

X-ray Reflectivity (XRR) was then used to measure the specular reflected portion of the signal in a butterfly-type scan in the small angle regime adjacent to the region of total external reflection. This gives insight into the surface normal electron density profile and can thus provide data to quantify the surface roughness, electron density and film thickness, without relying on the crystallinity of the material. **Figure 3i**) shows the evolution of the XRR signal due to hydrogenation (the curves are vertically shifted for clarity). By comparing the curves, three significant changes can be observed: i) the periodicity of the characteristic visible Kiessig fringes shortens[79]; ii) the amplitude of the fringes increases; and iii) the overall reflectivity decays much faster. Unfortunately, the feasibility of

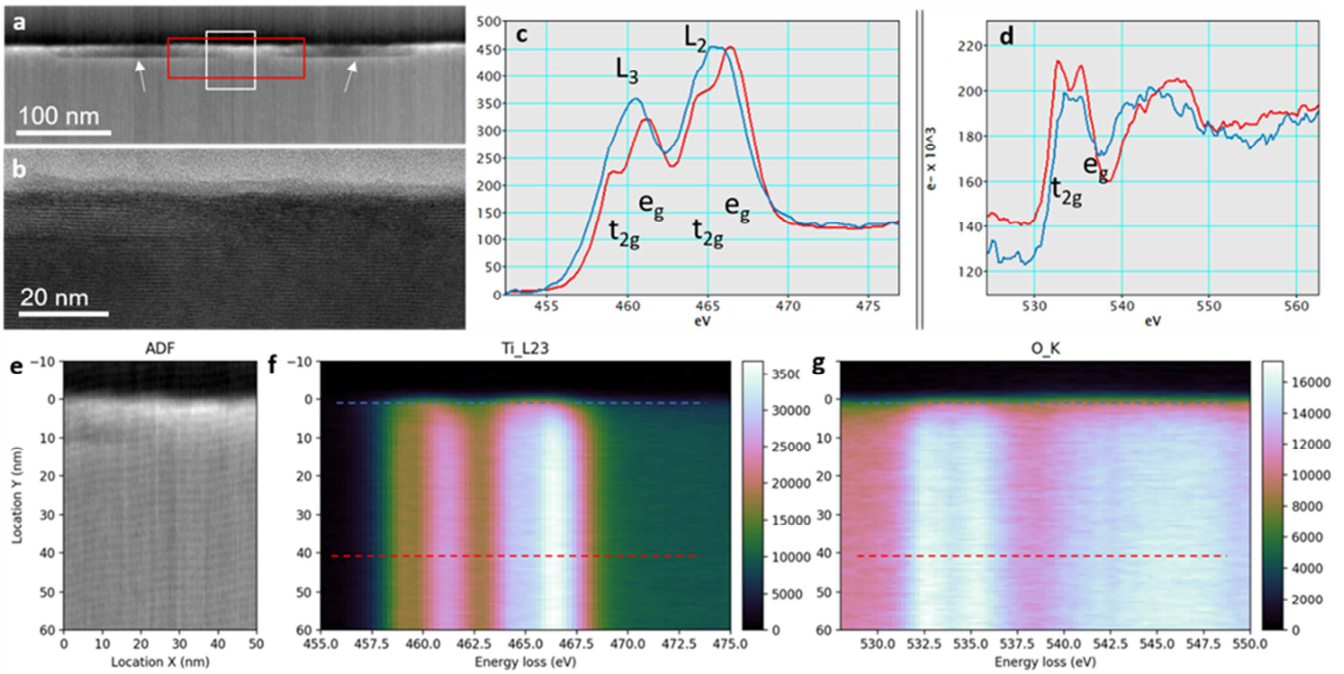

Figure 4 Spatially resolved EELS study of a cross-sectional specimen from the hydrogenated brookite single crystal. (a) STEM-ADF overview of a region, where STEM-EELS datasets (white box marked area, results in (c)-(g)) and HRTEM image (red box marked area) were acquired. The white arrows indicate the surface grooves. Simultaneously acquired STEM-ADF image (e) and EELS spectra of Ti-L23 (f) and O-K (g). Note the horizontal artificial stripes in (e) originate from a scanning Moiré. The original spectra datacube is rotated and projected, so that the new horizontal axis represents the energy loss and vertical axis correlates to the spatial location from bulk (bottom) to surface (top). Two spectra from the bulk and at the surface are extracted and shown in (c) and (d).

XRR modelling requires a horizontally homogeneous sample, which is an invalid assumption as demonstrated by the STEM images, thus no model-based fitting could be extrapolated from these results. However, the above-mentioned trends are directly correlated to changes taking place at the crystal surface. The thickness d of the structurally disorder surface layer can be estimated from the spacing Δq of adjacent minima via $d = \Delta q/2\pi$ (see blue vertical lines in **Figure 3i**), providing a vertical dimension of ~ 13.5 nm. The fringe amplitude stems from a change in the electron density, proving a reduced electron density in the disordered surface layer. Finally, the overall decay of the XRR curves originates from surface roughness, further supporting the formation of a rough surface layer during/upon hydrogenation.

In conclusion the combined electron and x-ray structural characterization of the specimens yields the consistent picture of an evolving inhomogeneous and rough crystalline surface layer with a vertical dimension of ~13 nm, composed of brookite phase, and featuring in-plane strain and a lower electron density. The vertical depth likely originates from pits and grooves at the surface, which can also be seen projected in the STEM images. In other words, hydrogenation slightly affects the surface crystallographic properties of brookite TiO2. Although the atoms are, in average, located as they would be in a pristine brookite lattice (as proven by diffraction, i.e. peak center position), likely several atoms at the surface are slightly displaced from their lattice position, which is proven by the increment of the peak intensity. This lattice distortion is ascribed to point defects as well as to surface grooves formed upon hydrogenation, which introduce strain fields.

Spatially resolved Electron Energy Loss Spectroscopy (EELS) datasets were acquired and analyzed, as presented in **Figure 4**. **Figure 4a** is a STEM-ADF cross-sectional image of the lamella prepared from the hydrogenated brookite single crystal. This lamella is the same from which the STEM-EELS datasets were acquired (from the white boxed region). Two surface grooves with a depth of about 10 nm can be clearly seen. A HRTEM image of the same area (red marked box in **Figure 4a**) is shown in **Figure 4b**. Within the grooves, the HRTEM show clear crystalline lattice contrast. The STEM-ADF-EELS datasets from the white-box marked region in **Figure 4a** is presented in **Figure 4e-g**. Two of the representative spectra, extracted from surface and bulk locations are shown in **Figure 4c** and **d**. The characteristic lines of Ti-L_{23} and O-K are clearly revealed, which originate from the excitation of 2p orbitals to the unoccupied 3d states that depend sensitively on the character of chemical bonds (i.e. environment of the crystal field, e.g. bonding symmetries, degeneracy of states, etc.). These fingerprint features in the fine structures are widely used to study the character of the chemical bonds.[80–83] In the bulk of the sample, the splitting of the doublet at the Ti-L_2 and Ti-L_3 is pronounced (which is designated to the t_{2g} and e_g orbitals, respectively, in the molecular orbital picture). This splitting originates from the mixing of final states owing to the crystal field from the neighboring ions, which causes lower degree of degeneracy and were forbidden in the spherical symmetry of the (hypothetical free-standing) titanium ions. The exact spilt and shift in energy, as well the relative ratio of the multiplets, provide fingerprint information about the bonding symmetry and bonding angle distortions. These results agree well to the reference spectra of brookite as presented in ref. [82]. The

splitting of the O-K is also in good agreement with the reference. In contrast, the spectra obtained from the surface show only the broad Ti-L_2, Ti-L_3 and O-K peaks without splitting into doublets, and the Ti-L_{23} peak shifted slightly toward lower energies. Such feature is expected for titanium ions with higher symmetry, such as titanium ions in an amorphous or strongly distorted crystalline phase. Indeed the spectra match reasonably well to that of crystalline Ti_2O_3.[80] These findings agree well with the presence of Ti^{3+} species as found by EPR in powders after hydrogenation at 500°C. Note that the thickness of this top surface layer depends strongly on the sample position: at another region of the sample, it exhibits for example a thickness of ~6 nm (see **Figure S10**).

The results, overall, suggest that to activate brookite for co-catalyst free H_2 evolution, the formation of an amorphous surface TiO_2 layer is not essential, in contrast to what has been proposed in previous work (e.g. "amorphous shell" in black TiO_2).[51,84]

Conclusions

This work shows that "mildly" reduced brookite produced under optimized hydrogenation conditions (pure H_2, 500°C, 10 min) can not only enable co-catalyst free photocatalytic H_2 evolution, as previously reported for anatase, but also provide an activity that is far superior to that of hydrogenated anatase. Hydrogenated rutile, in line with previous work, could not activate co-catalyst free H_2 evolution.

The photo-activity of hydrogenated brookite can be explained – as for anatase – by the introduction of suitable surface defect states. By a combination of powder and single crystal experiments based on TEM, Raman spectroscopy, XRD and XRR techniques, we show that such photocatalytically active defects are formed in brookite in a strained few nm thick surface region, without causing phase transition to rutile or amorphization effects. By EPR, we confirm that these defects are associated to V_Os and Ti^{3+} surface states, which act as mediators for electron transfer to H_2O to evolve H_2. The remarkable photocatalytic enhancement observed for brookite is ascribed to a CB edge that is energetically higher than that of anatase).[6,10,71] – thus providing a higher driving force for electron transfer from this polymorph.

Importantly, we also resolve a long-term debate, that is, the photocatalytic performance of reduced titania polymorphs, namely brookite or anatase, cannot be associated with the formation of an amorphous reduced TiO_2 "shell" or surface layer. Instead, structural features introduced by hydrogenation such as point defects, and possibly even crystallographic strain, play a key role towards co-catalyst free photocatalysis.

Acknowledgements

The authors would like to acknowledge the ERC, the DFG, and the DFG cluster of excellence "Engineering of Advanced Materials" for financial support. E.W. thanks the Alexander von Humboldt Foundation, Bonn, Germany, for funding the postdoctoral fellowship. J.W. and E.S. acknowledge the research training group GRK 1896 "In Situ Microscopy with Electrons, X-rays, and Scanning Probes". Dr. Shiva Mohajernia is gratefully acknowledged for Raman spectroscopy measurements and Dr. Nhat Truong Nguyen for TEM measurements.

Conflicts of interest

There are no conflicts to declare

References

1 A. Fujishima and K. Honda, *Nature*, 1972, **238**, 37–38.
2 A. L. Linsebigler, G. Lu and J. T. Yates, *Chem. Rev.*, 1995, **95**, 735–758.
3 M. R. Hoffmann, S. T. Martin, W. Choi and D. W. Bahnemann, *Chem. Rev.*, 1995, **95**, 69–96.
4 Z. Hengzhong and J. F. Banfield, *J. Phys. Chem. B*, 2000, **104**, 3481–3487.
5 Q. Tay, X. Liu, Y. Tang, Z. Jiang, T. C. Sum and Z. Chen, *J. Phys. Chem. C*, 2013, **117**, 14973–14982.
6 T. A. Kandiel, A. Feldhoff, L. Robben, R. Dillert and D. W. Bahnemann, *Chem. Mater.*, 2010, **22**, 2050–2060.
7 M. R. Ranade, A. Navrotsky, H. Z. Zhang, J. F. Banfield, S. H. Elder, A. Zaban, P. H. Borse, S. K. Kulkarni, G. S. Doran and H. J. Whitfield, *Proc. Natl. Acad. Sci.*, 2002, **99**, 6476–6481.
8 A. Beltram, I. Romero-Ocaña, J. Josè Delgado Jaen, T. Montini and P. Fornasiero, *Appl. Catal. A Gen.*, 2016, **518**, 167–175.
9 A. Di Paola, M. Bellardita and L. Palmisano, *Catalysts*, 2013, **3**, 36–73.
10 A. Di Paola, M. Bellardita, R. Ceccato, L. Palmisano and F. Parrino, *J. Phys. Chem. C*, 2009, **113**, 15166–15174.
11 A. Di Paola, G. Cufalo, M. Addamo, M. Bellardita, R. Campostrini, M. Ischia, R. Ceccato and L. Palmisano, *Colloids Surfaces A Physicochem. Eng. Asp.*, 2008, **317**, 366–376.
12 M. Altomare, M. V. Dozzi, G. L. Chiarello, A. Di Paola, L. Palmisano and E. Selli, *Catal. Today*, 2015, **252**, 184–189.
13 A. Naldoni, T. Montini, F. Malara, M. M. Mróz, A. Beltram, T. Virgili, C. L. Boldrini, M. Marelli, I. Romero-Ocaña, J. J. Delgado, V. Dal Santo and P. Fornasiero, *ACS Catal.*, 2017, **7**, 1270–1278.
14 J. Cihlar, V. Kasparek, M. Kralova and K. Castkova, *Int. J. Hydrogen Energy*, 2015, **40**, 2950–2962.
15 I. Romero Ocaña, A. Beltram, J. J. Delgado Jaén, G. Adami, T. Montini and P. Fornasiero, *Inorganica Chim. Acta*, 2015, **431**, 197–205.
16 G. L. Chiarello, A. Di Paola, L. Palmisano and E. Selli, *Photochem. Photobiol. Sci.*, 2011, **10**, 355–360.
17 M. Bellardita, E. I. García-López, G. Marcì and L. Palmisano, *Int. J. Hydrogen Energy*, 2016, **41**, 5934–5947.
18 M. Hezam, S. M. H. Qaid, I. M. Bedja, F. Alharbi, M. K. Nazeeruddin and A. Aldwayyan, *Crystals*, 2019, **9**, 562.
19 H. Zhao, L. Liu, J. M. Andino and Y. Li, *J. Mater. Chem. A*,

2013, **1**, 8209–8216.
20 G. R. Bamwenda, S. Tsubota, T. Kobayashi and M. Haruta, *J. Photochem. Photobiol. A Chem.*, 1994, **77**, 59–67.
21 G. L. Chiarello, M. H. Aguirre and E. Selli, *J. Catal.*, 2010, **273**, 182–190.
22 A. Naldoni, M. D'Arienzo, M. Altomare, M. Marelli, R. Scotti, F. Morazzoni, E. Selli and V. Dal Santo, *Appl. Catal. B Environ.*, 2013, **130**–**131**, 239–248.
23 D. Spanu, S. Recchia, S. Mohajernia, O. Tomanec, Š. Kment, R. Zboril, P. Schmuki and M. Altomare, *ACS Catal.*, 2018, **8**, 5298–5305.
24 A. Meng, L. Zhang, B. Cheng and J. Yu, *Adv. Mater.*, 2019, **31**, 1807660.
25 D. Spanu, A. Minguzzi, S. Recchia, F. Shahvardanfard, O. Tomanec, R. Zboril, P. Schmuki, P. Ghigna and M. Altomare, *ACS Catal.*, 2020, **10**, 8293–8302.
26 F. Shahvaranfard, P. Ghigna, A. Minguzzi, E. Wierzbicka, P. Schmuki and M. Altomare, *ACS Appl. Mater. Interfaces*, 2020, **12**, 38211–38221.
27 Z. Zhang and J. T. Yates, *Chem. Rev.*, 2012, **112**, 5520–5551.
28 J. B. Joo, R. Dillon, I. Lee, Y. Yin, C. J. Bardeen and F. Zaera, *Proc. Natl. Acad. Sci.*, 2014, **111**, 7942–7947.
29 M. Wajid Shah, Y. Zhu, X. Fan, J. Zhao, Y. Li, S. Asim and C. Wang, *Sci. Rep.*, 2015, **5**, 1–8.
30 B. Bharti, S. Kumar, H. N. Lee and R. Kumar, *Sci. Rep.*, 2016, **6**, 1–12.
31 F. Zuo, L. Wang, T. Wu, Z. Zhang, D. Borchardt and P. Feng, *J. Am. Chem. Soc.*, 2010, **132**, 11856–11857.
32 M. Xing, W. Fang, M. Nasir, Y. Ma, J. Zhang and M. Anpo, *J. Catal.*, 2013, **297**, 236–243.
33 A. Naldoni, M. Altomare, G. Zoppellaro, N. Liu, Š. Kment, R. Zbořil and P. Schmuki, *ACS Catal.*, 2019, **9**, 345–364.
34 X. Zhou, N. Liu, J. Schmidt, A. Kahnt, A. Osvet, S. Romeis, E. M. Zolnhofer, V. R. R. Marthala, D. M. Guldi, W. Peukert, M. Hartmann, K. Meyer and P. Schmuki, *Adv. Mater.*, 2017, **29**, 1604747.
35 N. Liu, V. Häublein, X. Zhou, U. Venkatesan, M. Hartmann, M. MačKović, T. Nakajima, E. Spiecker, A. Osvet, L. Frey and P. Schmuki, *Nano Lett.*, 2015, **15**, 6815–6820.
36 E. Wierzbicka, X. Zhou, N. Denisov, J. E. Yoo, D. Fehn, N. Liu, K. Meyer and P. Schmuki, *ChemSusChem*, 2019, **12**, 1900–1905.
37 A. Naldoni, M. Allieta, S. Santangelo, M. Marelli, F. Fabbri, S. Cappelli, C. L. Bianchi, R. Psaro, V. Dal Santo and V. D. Santo, *J. Am. Chem. Soc.*, 2012, **134**, 7600–7603.
38 G. Zhu, T. Lin, X. Lü, W. Zhao, C. Yang, Z. Wang, H. Yin, Z. Liu, F. Huang and J. Lin, *J. Mater. Chem. A*, 2013, **1**, 9650–9653.
39 N. Liu, C. Schneider, D. Freitag, U. Venkatesan, V. R. R. Marthala, M. Hartmann, B. Winter, E. Spiecker, A. Osvet, E. M. Zolnhofer, K. Meyer, T. Nakajima, X. Zhou and P. Schmuki, *Angew. Chem. Int. Ed. Engl.*, 2014, **126**, 14425–14429.
40 N. Liu, X. Zhou, N. T. Nguyen, K. Peters, F. Zoller, I. Hwang, C. Schneider, M. E. Miehlich, D. Freitag, K. Meyer, D. Fattakhova-Rohlfing and P. Schmuki, *ChemSusChem*, 2017, **10**, 62–67.
41 X. Zhou, E. Wierzbicka, N. Liu and P. Schmuki, *Chem. Commun.*, 2019, **55**, 533–536.
42 N. Liu, C. Schneider, D. Freitag, M. Hartmann, U. Venkatesan, J. Müller, E. Spiecker and P. Schmuki, *Nano Lett.*, 2014, **14**, 3309–3313.
43 N. Liu, H. G. Steinrück, A. Osvet, Y. Yang and P. Schmuki, *Appl. Phys. Lett.*, 2017, **110**, 072102.
44 J. J. M. Vequizo, H. Matsunaga, T. Ishiku, S. Kamimura, T. Ohno and A. Yamakata, *ACS Catal.*, 2017, **7**, 2644–2651.
45 A. Yamakata and J. J. M. Vequizo, *J. Photochem. Photobiol. C Photochem. Rev.*, 2019, **40**, 234–243.
46 C. Di Valentin, G. Pacchioni and A. Selloni, *J. Phys. Chem. C*, 2009, **113**, 20543–20552.
47 B. J. Morgan and G. W. Watson, *J. Phys. Chem. C*, 2010, **114**, 2321–2328.
48 D. C. Cronemeyer, *Phys. Rev.*, 1959, **113**, 1222–1226.
49 J. Schneider, M. Matsuoka, M. Takeuchi, J. Zhang, Y. Horiuchi, M. Anpo and D. W. Bahnemann, *Chem. Rev.*, 2014, **114**, 9919–9986.
50 Y. Ma, X. Wang, Y. Jia, X. Chen, H. Han and C. Li, *Chem. Rev.*, 2014, **114**, 9987–10043.
51 X. Chen, L. Liu, P. Y. Yu and S. S. Mao, *Science*, 2011, **331**, 746–750.
52 A. Naldoni, F. Fabbri, M. Altomare, M. Marelli, R. Psaro, E. Selli, G. Salvati and V. D. Santo, *Phys. Chem. Chem. Phys.*, 2015, **17**, 4864–4869.
53 T. Takata, J. Jiang, Y. Sakata, M. Nakabayashi, N. Shibata, V. Nandal, K. Seki, T. Hisatomi and K. Domen, *Nature*, 2020, **581**, 411–414.
54 A. Kudo and Y. Miseki, *Chem. Soc. Rev.*, 2009, **38**, 253–278.
55 S. Chen, T. Takata and K. Domen, *Nat. Rev. Mater.*, 2017, **2**, 17050.
56 U. Diebold, *Surf. Sci. Rep.*, 2003, **48**, 53–229.
57 L. Jiang, Y. Li, H. Yang, Y. Yang, J. Liu, Z. Yan, X. Long, J. He and J. Wang, *Catalysts*, 2017, **7**, 376.
58 X. Xin, T. Xu, L. Wang and C. Wang, *Sci. Rep.*, 2016, **6**, 23684.
59 S. Livraghi, M. Rolando, S. Maurelli, M. Chiesa, M. C. Paganini and E. Giamello, *J. Phys. Chem. C*, 2014, **118**, 22141–22148.
60 M. Cargnello, T. Montini, S. Y. Smolin, J. B. Priebe, J. J. D. Jaén, V. V. T. Doan-Nguyen, I. S. McKay, J. A. Schwalbe, M. M. Pohl, T. R. Gordon, Y. Lu, J. B. Baxter, A. Brückner, P. Fornasiero and C. B. Murray, *Proc. Natl. Acad. Sci. U. S. A.*, 2016, **113**, 3966–3971.
61 M. Chiesa, M. C. Paganini, S. Livraghi and E. Giamello, *Phys. Chem. Chem. Phys.*, 2013, **15**, 9435–9447.
62 S. Mohajernia, P. Andryskova, G. Zoppellaro, S. Hejazi, S. Kment, R. Zboril, J. Schmidt and P. Schmuki, *J. Mater. Chem. A*, 2020, **8**, 1432–1442.
63 J. E. Yoo, A. A. Alshehri, S. Qin, S. M. Bawaked, M. M. M. Mostafa, N. Katabathini, D. Fehn, J. Schmidt, A. Mazare, N. Denisov, G. Cha, K. Meyer and P. Schmuki, *ChemCatChem*, 2020, **12**, 2951–2956.
64 N. A. Deskins, R. Rousseau and M. Dupuis, *J. Phys. Chem. C*, 2011, **115**, 7562–7572.
65 M. Aono and R. R. Hasiguti, *Phys. Rev. B*, 1993, **48**, 12406–

12414.
66 X. Pan, M. Q. Yang, X. Fu, N. Zhang and Y. J. Xu, *Nanoscale*, 2013, **5**, 3601–3614.
67 N. Liu, C. Schneider, D. Freitag, M. Hartmann, U. Venkatesan, J. Müller, E. Spiecker and P. Schmuki, *Nano Lett.*, 2014, **14**, 3309–3313.
68 S. Mohajernia, S. Hejazi, A. Mazare, N. T. Nguyen and P. Schmuki, *Chem. - A Eur. J.*, 2017, **23**, 12406–12411.
69 G. A. Tompsett, G. A. Bowmaker, R. P. Cooney, J. B. Metson, K. A. Rodgers and J. M. Seakins, *J. Raman Spectrosc*, 1995, **26**, 57–62.
70 H. C. Choi, Y. M. Jung and S. Bin Kim, *Vib. Spectrosc.*, 2005, **37**, 33–38.
71 Q. Tay, X. Wang, X. Zhao, J. Hong, Q. Zhang, R. Xu and Z. Chen, *J. Catal.*, 2016, **342**, 55–62.
72 D. Y. C. Leung, X. Fu, C. Wang, M. Ni and M. K. H. Leung, , DOI:10.1002/cssc.201000014.
73 S. J. Pennycook, *Ultramicroscopy*, 1989, **30**, 58–69.
74 L. Pauling and J. H. Sturdivant, *Zeitschrift für Krist. Mater.*, 1928, **68**, 239–256.
75 J. M. Cowley, *Diffraction physics*, Elsevier, North Holland, 3rd edn., 1995.
76 J. Daillant and A. Gibaud, *X-ray and neutron reflectivity: principles and applications*, Springer, 2008, vol. 770.
77 W. H. Baur and A. A. Khan, *Acta Crystallogr. Sect. B Struct. Crystallogr. Cryst. Chem.*, 1971, **27**, 2133–2139.
78 H. Dosch, *Critical phenomena at surfaces and interfaces: evanescent X-ray and neutron scattering*, Springer, 2006, vol. 126.
79 H. Kiessig, *Ann. Phys.*, 1931, **402**, 769–788.
80 E. Stoyanov, F. Langenhorst and G. Steinle-Neumann, *Am. Mineral.*, 2007, **92**, 577–586.
81 V. J. Keast, A. J. Scott, R. Brydson, D. B. Williams and J. Bruley, *J. Microsc.*, 2001, **203**, 135–175.
82 C. Heiliger, F. Heyroth, F. Syrowatka, H. S. Leipner, I. Maznichenko, K. Kokko, W. Hergert and I. Mertig, *Phys. Rev. B*, 2006, **73**, 45129.
83 A. Tafel, M. Wu, E. Spiecker, P. Hommelhoff and J. Ristein, *Diam. Relat. Mater.*, 2019, **97**, 107446.
84 L. Liu and X. Chen, *Chem. Rev.*, 2014, **114**, 9890–9918.

